Applied Thermal Engineering 300 (2026) 131220

Contents lists available at ScienceDirect

Applied Thermal Engineering

journal homepage: www.elsevier.com/locate/ate

Research Paper

Optimization of packed-bed sensible heat storage systems based on a second law analysis

Yan Jin *, Evgenia Makhova, Arne Speerforck

Institute of Engineering Thermodynamics, Hamburg University of Technology, Hamburg 21073, Germany

ARTICLE INFO

Keywords:
Thermal energy storage
Second law analysis
Computational fluid dynamics
Porous media
Exergy
Sensible heat storage

ABSTRACT

Packed-bed sensible heat storage (SHS) is important for balancing energy supply and demand over time. To improve the efficiency of a packed-bed SHS system through second law analysis (SLA), we developed multi-dimensional macroscopic entropy and exergy transport equations for fluid flow and heat transfer in porous media. These equations enable us to identify where and how much exergy is destroyed. Using a packed-bed SHS system developed at the PROMES-CNRS laboratory as a test case, we demonstrated how to apply SLA to optimize an SHS system. Our analysis revealed that, in addition to exit and heat leakage losses at tank surfaces, thermal and solid conduction losses inside the tank significantly contribute to total loss in the studied SHS system. These internal losses occur close to the thermocline. However, their slower transport causes a delay in their emergence. The SLA suggests an optimal tank aspect ratio of $D/H = 0.75$, at which the total exergy loss coefficient, ζ_{tot}^{b}, reaches its minimum value when exit loss is not considered. As particle size decreases, ζ_{tot}^{b} also decreases due to enhanced heat transfer between the fluid and solid phases. The pressure loss for the studied SHS system is found to be negligible. The SLA favors a truncated cone-shaped tank with a slightly larger upper surface. Through the SLA, ζ_{tot}^{b} is reduced by approximately 16.3% from 4.9% for the original design to 4.1% for the optimized design. This study demonstrates that, when used in conjunction with energy analysis, the SLA is an effective tool for optimizing energy storage systems.

1. Introduction

Thermal energy storage (TES) is a technology that enables the storage of thermal energy for later use in heating, cooling or power generation applications. It helps bridge the temporal mismatch between energy supply and demand. TES is important for using intermittent renewable energies such as solar and wind energy, which are not always produced when needed. The development of efficient TES systems is therefore important for improving overall system-level efficiency, reducing environmental impact, and providing low-cost energy.

There are three main types of TES systems: sensible heat storage (SHS), which stores thermal energy by raising or lowering the temperature of a storage material without changing its phase, latent heat storage (LHS), which stores thermal energy through the phase change of a material, and thermochemical heat storage (TCHS), which stores thermal energy through reversible chemical reactions or sorption processes [1–3]. Among these, SHS is regarded as the most established and straightforward thermal energy storage technology. In an SHS system, thermal energy is stored or released by raising or lowering the temperature of thermal energy storage materials (TESMs). These materials can be stored in either one or two tanks [4,5]. This study focuses on one-tank SHS systems. In these systems, hot fluid is introduced from the top during charging and cold fluid is introduced from the bottom during discharging. Consequently, a thermal gradient, or thermocline, occurs between the hot and cold zones in the tank. Thus, this system is also referred to as a thermocline thermal energy storage (TTES) system [6], as illustrated in Fig. 1.

While liquid thermal energy storage materials (TESM) are commonly employed in SHS systems, solid materials are sometimes incorporated into the tank to partially replace the liquid TESM. This configuration, known as a packed-bed one-tank SHS [7]. This further reduces the cost of the TES. Additionally, solid filler materials are also used to increase effective heat capacity, enhance regenerative heat transfer, improve thermocline formation, and increase heat transfer area. However, the solid particles also make the fluid flow and heat transfer inside the tank more complicated. The relevant parameters that have been studied in the literature include tank height L, tank diameter D, porosity ϕ, particle diameter d_p, heat transfer fluid (HTF) mass flow rate $\dot{m}$, HTF cold and hot temperatures T_c and T_h, TESM properties, etc. [6,8–10]. In addition to these parameters, transport processes in packed-bed energy storage systems may also depend on pore geometry,

* Corresponding author.
E-mail address: yan.jin@tuhh.de (Y. Jin).

https://doi.org/10.1016/j.applthermaleng.2026.131220
Received 27 January 2026; Received in revised form 31 March 2026; Accepted 26 April 2026
Available online 29 April 2026

Nomenclature

Roman letters

$\dot{L}$	Loss rate, W
$\dot{l}$	Loss rate intensity, $W\,m^{-3}$
A	Tank surface area, m^2
B	Exergy, J
b	Specific exergy, $J\,kg^{-1}$
C_p	Heat capacity, $J\,kg^{-1}\,K^{-1}$
D	Tank diameter, m
D_0	Equivalent tank diameter, m
D_1	Upper surface diameter of a truncated-cone shaped tank, m
D_2	Lower surface diameter of a truncated-cone shaped tank, m
d_p	Particle size, m
e	Specific energy, $J\,kg^{-1}$
h	Specific enthalpy, $J\,kg^{-1}$
H	Tank height, m
K	Permeability, m^2
k	Heat conductivity, $W\,m^{-1}K^{-1}$
Q	Thermal energy, J
R_{th}	Thermal resistance, $K\,W^{-1}$
s	Specific entropy, $J\,kg^{-1}\,K^{-1}$
T	Temperature, K
t	Time, s

Greek symbols

α	Heat transfer coefficient, $W\,m^{-2}K^{-1}$
η	Storage efficiency, –
μ	Dynamic viscosity, Pa s
ϕ	Porosity, –
ρ	Density, $kg\,m^{-3}$
ζ	Loss coefficient, –

Superscripts

b	Exergy
e	Energy
mac	Macroscopic
mic	Microscopic

Subscripts

bot	Tank bottom surface
chg	Charge
cyc	Charge–discharge cycle
dis	Discharge
f	Fluid
hsf	Heat transfer between fluid and solid
htf	Heat conduction in fluid
hts	Heat conduction in solid
I	The first law
II	The second law
opt	Optimized
oth	Others
pre	Pressure
s	Solid
tot	Total
vol	Tank volume
w, wal	Tank wall

Abbreviations

CFD	Computational fluid dynamics
HTF	Heat transfer fluid
SHS	Sensible heat storage
SLA	Second law analysis
TCHS	Thermo-chemical heat storage
TES	Thermal energy storage
TESM	Thermal energy storage material

spatial distribution, and other structural characteristics of the porous medium. Research on these parameters remains insufficient.

SHS systems can be studied using various methods, including experimental and numerical approaches. One-dimensional simulations are most often used among the numerical simulations due to their low computational cost. Hoffmann, et al. (2016) [6] argue that a one-dimensional model is sufficient to describe the general behavior of an SHS system. However, some studies use multi-dimensional computational fluid dynamics (CFD) simulations to investigate the flow and temperature fields in more detail. Many CFD studies have been conducted to improve the understanding of thermal stratification during charging and discharging. For instance, Zachar, et al. (2003) examined the impact of various plate sizes positioned opposite the inlet to enhance thermal stratification [11]. They found that the diameter of the plate and the distance between the plate and the top of the tank have a significant effect on the temperature stratification within the tank when cold water enters at the top of the tank. Göppert, et al. (2009) proposed an efficient CFD method to study the impact of geometry on thermal stratification [12]. This method considerably reduces computational costs. Kursun (2018) studied the effect of insulation geometries on thermal stratification and proposed a novel geometry to enhance it [13]. With the optimized geometry, the maximum water temperature difference in the tanks increases by 85–138%. Li, et al. (2018) found that a truncated circular cone tank has the best temperature stratification and thermal charging efficiency [14]. Gao, et al. (2021) investigated the effect of a baffle plate on thermal stratification characteristics [15]. Based on the numerical and experimental results, they have proposed the optimized baffle position, aperture and inlet velocity. Hosseinnia, et al. (2021) simulated thermocline evolution during the charging phase of a stratified thermal energy storage tank. Their numerical results show that an ideal diffuser generates the minimum charging velocity with no mixing or turbulence [16].

CFD simulations were also used to study the effect of other parameters of SHS systems. For instance, Cascetta, et al. (2016) compared CFD and experimental results from a sensible thermal energy storage system. They indicated that the thermal properties of both phases must be temperature-dependent in the simulation to achieve high accuracy [17]. Khan, et al. (2019) simulated the initial charge–discharge cycle of an SHS system consisting of rocks and pebbles poured into a mild steel tank and validated the numerical results with experimental data [18]. Andreozzi, et al. (2014) simulated the charge and discharge cycles of high-temperature thermal storage in a honeycomb solid matrix [19]. They analyzed the effects of the storage medium, different porosity values, and mass flow rate on stored thermal energy and storage time based on the numerical results. The numerical results suggest that an optimal porosity value could be evaluated by accounting for the pressure drop and the viscous dissipation inside the system. Elfeky, et al. (2021) investigated the performance of an air-rock thermocline thermal energy storage (TES) tank for concentrated solar power plants using a coupled discrete element method (DEM)-computational fluid dynamics (CFD) approach. Their numerical results show that a HTF

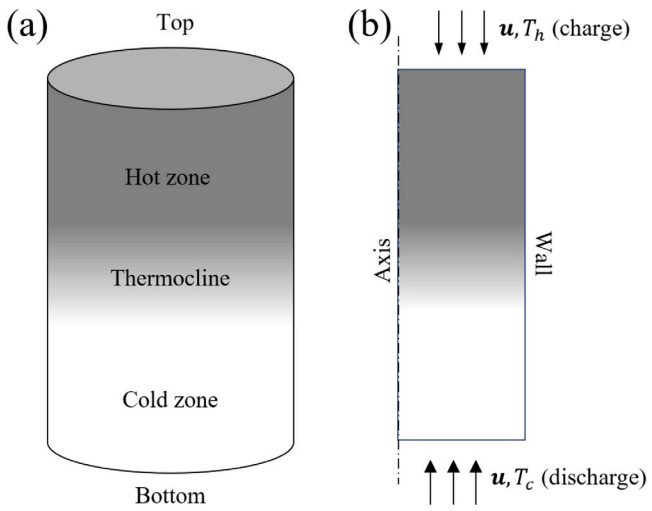

Fig. 1. Schematic illustration of a packed-bed thermal store (a) and the corresponding two-dimensional axisymmetric computational domain (b).

distributor can reduce the heat leakage at the wall [20]. In their comprehensive review of CFD studies on SHS systems, Chekifi and Boukraa (2023) [21] conclude that CFD is a powerful tool for understanding the effects of relevant parameters and optimizing system performance.

It can be observed that most numerical studies focus on the storage efficiency based on the first law of thermodynamics. In particular these studies often only consider the loss of the thermal energy. The corresponding storage efficiency is defined as,

$$\eta_I = \frac{Q_{dis}}{Q_{chg}}, \tag{1}$$

where Q_{dis} is the quantity of thermal energy that is extracted during discharge and Q_{chg} is the thermal energy entering the store during charge [8]. However, this definition neglects the difference of the energy quality, meaning that the same amount of thermal energy but at different temperatures may produce different amounts of work. To assess the difference in energy quality, one must consider the loss of exergy using the second law of thermodynamics.

Some works about using the second law analysis (SLA) to study the packed-bed thermal reservoirs exist in the literature. According to the SLA, the efficiency of an SHS system should be evaluated based on the exergy loss, which is defined as

$$\eta_{II} = \frac{B_{dis}}{B_{chg}}, \tag{2}$$

where B_{dis} is the quantity of exergy that is extracted during discharge and B_{chg} is the exergy entering the store during charge. White, et al. (2011) demonstrate the dependence of the losses on operating temperatures, reservoir geometry and mode of operation, and suggest methods of optimization [9]. In a later study, White, et al. (2014) suggest that the changes in specific heat capacity result in non-linear wave propagation, which may lead to the formation of shock-like thermal fronts. This has a significant impact on the exergetic losses due to irreversible heat transfer [22]. They have also analyzed the effect of segmenting the packed-bed into layers on exergy losses [10,23]. The study shows that segmentation of the packed beds is an effective way to attain high storage efficiency and fully utilize of the reservoirs. The TES system was optimized based on the SLA [24]. After optimization, losses due to pressure drop and irreversible heat transfer in the thermal reservoirs are reduced to a few percent. Abdulla and Reddy (2017) suggest that reduction in efficiency at higher temperature difference corresponds to higher value of exergy destruction inside the tank [25]. McTigue, et al. (2018) compared the exergy losses of radial-flow and axial-flow packed beds for thermal energy storage, indicating that both designs have comparable thermodynamic performance [26]. They have also found that segmenting the packed bed into layers reduces the effect of perturbations during charge–discharge cycles [27].

These studies demonstrate the potential of using the SLA to optimize SHS systems. However, they are typically based on one-dimensional system simulation results. Herwig (2012) [28] states that the SLA can be used to answer four important questions concerning a momentum and/or heat transfer process. They are "Which is the ideal process (no entropy generation)? Where does entropy generation occur in a non-ideal process? Why does entropy generation occur at a certain location and with certain strength? How can entropy generation be reduced overall or locally?" The answers to these questions are important for optimizing SHS systems. However, to address these questions, multi-dimensional (two- or three-dimensional) simulations of fluid flow and heat transfer over extended periods (typically several hours or longer) are required, often demanding substantial computational resources. Additionally, developing multi-dimensional entropy and exergy transport equations in an SHS system is important for evaluating local entropy generation and exergy destruction intensities. Entropy and exergy transport in an SHS system is more complicated than in pure flow and heat transfer problems because the effect of the packed bed (modeled as a porous medium) has to be considered. There is still a lack of derivation of the multi-dimensional macroscopic entropy and exergy transport equations for fluid flow and heat transfer in porous media from the microscopic equations.

The primary objective of this work is to develop and apply multi-dimensional macroscopic entropy and exergy transport equations to identify and quantify the irreversibilities in packed-bed sensible heat storage systems. Parametric studies of an SHS system are presented as applications of the proposed framework to demonstrate how the method can be used to analyze exergy destruction and improve storage performance. The fundamental questions posed by Herwig (2012) [28] will be answered for the SHS system studied. The paper is structured as follows: After the introduction, Section 2 introduces the governing equations for multi-dimensional computational fluid dynamics (CFD) simulations of fluid flow and heat transfer problems in a porous medium. The macroscopic entropy and exergy transport equations are derived in this section. The application of the developed framework is demonstrated in Section 3, in which the test cases are introduced, and Section 4, in which results of application are discussed. Finally, Section 5 provides the conclusions.

2. Mathematical equations and numerical methods

2.1. Microscopic transport equations

We start from the governing equations for pore-scale resolved microscopic simulations of the charging and discharging processes in a packed-bed energy storage system. They are the classic equations for mass (3), momentum (4), and energy conservation in both the fluid (5) and solid (6) phases. These equations can be expressed as follows:

$$\frac{\partial \rho_f}{\partial t} + \frac{\partial \left(\rho_f u_i\right)}{\partial x_i} = 0, \tag{3}$$

$$\rho_f \frac{du_i}{dt} = \frac{\partial \left(\rho_f u_i\right)}{\partial t} + \frac{\partial \left(\rho_f u_j u_i\right)}{\partial x_j} = -\frac{\partial p}{\partial x_i} + \frac{\partial \tau_{ji}}{\partial x_j} + \rho_f g_i, \tag{4}$$

$$\rho_f \frac{dh_f}{dt} = \frac{\partial \left(\rho_f h_f\right)}{\partial t} + \frac{\partial \left(\rho_f u_i h_f\right)}{\partial x_i} = \frac{dp}{dt} + \frac{\partial}{\partial x_i}\left(k_f \frac{\partial T_f}{\partial x_i}\right) + \tau_{ji}\frac{\partial u_i}{\partial x_j}, \tag{5}$$

$$\rho_s \frac{de_s}{dt} = \frac{\partial}{\partial x_i}\left(k_s \frac{\partial T_s}{\partial x_i}\right). \tag{6}$$

ρ_f, u_i, τ_{ji}, h_f and k_f in the governing equations denote the density, velocity component, viscous stress, specific enthalpy and thermal conductivity in the fluid phase, respectively. ρ_s, e_s and k_s denote the

density, energy and thermal conductivity in the solid phase, respectively. Similar microscopic equations (excluding the energy equation in the solid phase) have been solved in our previous pore-scale resolved numerical simulations of convection in porous medium [29–32]. However, directly solving these equations for packed-bed thermal energy storage systems would be computationally very expensive. Therefore, these equations are introduced primarily as the theoretical foundation for the subsequent volume-averaging procedure, from which the macroscopic governing equations are derived. Multiplying Eq. (4) with u_i, the transport equation of the kinetic energy $k = \frac{1}{2}u_i^2$ can be obtained in the fluid phase, expressed as,

$$\rho_f \frac{dk}{dt} = \frac{\partial\left(\rho_f k\right)}{\partial t} + \frac{\partial\left(\rho_f u_i k\right)}{\partial x_i} = -u_i \frac{\partial p}{\partial x_i} + u_i \frac{\partial \tau_{ji}}{\partial x_j} + \rho_f u_i g_i, \tag{7}$$

For a Newtonian fluid, the viscous stress is calculated as

$$\tau_{ij} = 2\mu\left(s_{ij} - \frac{2}{3}\delta_{ij}\frac{\partial u_k}{\partial x_k}\right) + \eta\delta_{ij}\frac{\partial u_k}{\partial x_k}, \tag{8}$$

where s_{ij} is the strain rate tensor. μ and η stay for the shear viscosity and bulk viscosity, respectively. For an ideal gas the following equation of state is used:

$$\rho_f = p/\left(RT_f\right), \tag{9}$$

where R is the specific gas constant. Instead of Eq. (9), a constant fluid density ρ_f is used for an incompressible fluid.

Considering the fundamental equation of thermodynamics $dh_f = T_f ds_f + \frac{1}{\rho_f}dp$, there are

$$\frac{dh_f}{dt} = T_f \frac{ds_f}{dt} + \frac{1}{\rho}\frac{dp}{dt}, \tag{10}$$

for the fluid phase and

$$\frac{dh_s}{dt} = T_s \frac{ds_s}{dt}, \tag{11}$$

for the solid phase. Here, s_f and s_s represent the specific entropies of the fluid and solid phases, respectively. By substituting Eqs. (5) and (6) into Eqs. (10) and (11), we can obtain the following transport equations of entropy in the fluid and solid phases:

$$\rho_f \frac{ds_f}{dt} = \frac{\partial\left(\rho_f s_f\right)}{\partial t} + \frac{\partial\left(\rho_f u_i s_f\right)}{\partial x_i} = \frac{\partial}{\partial x_i}\left(\frac{k_f}{T_f}\frac{\partial T_f}{\partial x_i}\right) + \frac{k_f}{T_f^2}\frac{\partial T_f}{\partial x_i}\frac{\partial T_f}{\partial x_i} + \frac{\tau_{ji}s_{ji}}{T_f}, \tag{12}$$

$$\rho_s \frac{ds_s}{dt} = \frac{\partial}{\partial x_i}\left(\frac{k_s}{T_s}\frac{\partial T_s}{\partial x_i}\right) + \frac{k_s}{T_s^2}\frac{\partial T_s}{\partial x_i}\frac{\partial T_s}{\partial x_i}. \tag{13}$$

Here, $\dot{s}_{htf}^{mic} = \frac{k_f}{T_f^2}\frac{\partial T_f}{\partial x_i}\frac{\partial T_f}{\partial x_i}$ and $\dot{s}_{pre}^{mic} = \frac{\tau_{ji}s_{ji}}{T_f}$ are the entropy generation intensities in the temperature and flow fields of the fluid phase. $\dot{s}_{hts}^{mic} = \frac{k_s}{T_s^2}\frac{\partial T_s}{\partial x_i}\frac{\partial T_s}{\partial x_i}$ is the entropy generation intensity in the temperature field of the solid phase. Hereby, we assume ideal contact between the fluid and solid phases and neglect any interfacial irreversibilities that could arise from imperfect contact or microscale roughness.

Dividing the exergy difference in the fluid phase, $db_f = dh_f - T_0 ds_f + dk$, and in the solid phase $db_s = dh_s - T_0 ds_s$ by dt, we can obtain

$$\frac{db_f}{dt} = \frac{dh_f}{dt} - T_0\frac{ds_f}{dt} + \frac{dk}{dt}, \tag{14}$$

for the fluid phase and

$$\frac{db_s}{dt} = \frac{de_s}{dt} - T_0\frac{ds_s}{dt}, \tag{15}$$

for the solid phase. b_f and b_s are the specific exergy in the fluid and solid phases, respectively. Substituting Eqs. (5), (12) and (7) into Eq. (14), the following transport equation of the exergy in the fluid phase can be obtained,

$$\rho_f \frac{db_f}{dt} = \frac{\partial\left(\rho_f b_f\right)}{\partial t} + \frac{\partial\left(\rho_f u_i b_f\right)}{\partial x_i} = \frac{\partial p}{\partial t} + \frac{\partial}{\partial x_i}\left(k_f\left(1 - \frac{T_0}{T_f}\right)\frac{\partial T_f}{\partial x_i}\right) + \frac{\partial}{\partial x_j}\left(u_i\tau_{ji}\right) - T_0\left(\dot{s}_{htf}^{mic} + \dot{s}_{pre}^{mic}\right). \tag{16}$$

Similarly, substituting Eqs. (6) and (13) into Eq. (15) leads to the exergy transport equation in the solid phase,

$$\rho_s \frac{db_s}{dt} = \frac{\partial}{\partial x_i}\left(k_s\left(1 - \frac{T_0}{T_s}\right)\frac{\partial T_s}{\partial x_i}\right) - T_0\dot{s}_{hts}^{mic}. \tag{17}$$

2.2. Macroscopic transport equations

Taking the volume averaging of the microscopic governing Eqs. (3)–(6) in a representative elementary volume (REV), defined as smallest volume over which a volume-averaged measurement becomes independent of further increases in the averaging volume, leads to the macroscopic governing equations, expressed as

$$\frac{\partial\left(\phi\left\langle\rho_f\right\rangle^f\right)}{\partial t} + \frac{\partial\left(\phi\left\langle\rho_f\right\rangle^f\left\langle u_i\right\rangle^f\right)}{\partial x_i} = 0, \tag{18}$$

$$\left\langle\rho_f\frac{du_i}{dt}\right\rangle = \frac{\partial\left(\phi\left\langle\rho_f\right\rangle^f\left\langle u_i\right\rangle^f\right)}{\partial t} + \frac{\partial\left(\phi\left\langle\rho_f\right\rangle^f\left\langle u_j\right\rangle^f\left\langle u_i\right\rangle^f\right)}{\partial x_j} = -\phi\frac{\partial\langle p\rangle^f}{\partial x_i} + \phi\frac{\partial\left\langle\tau_{ji}\right\rangle^f}{\partial x_j} + \phi\left\langle\rho_f\right\rangle^f g_i + \phi F_i, \tag{19}$$

$$\left\langle\rho_f\frac{dh_f}{dt}\right\rangle = \frac{\partial\left(\phi\left\langle\rho_f\right\rangle^f\left\langle h_f\right\rangle^f\right)}{\partial t} + \frac{\partial\left(\phi\left\langle\rho_f\right\rangle^f\left\langle u_i\right\rangle^f\left\langle h_f\right\rangle^f\right)}{\partial x_i} = \phi\frac{\partial\langle p\rangle^f}{\partial t} + \phi\left\langle u_i\right\rangle^f\frac{\partial\langle p\rangle^f}{\partial x_i} + \frac{\partial}{\partial x_i}\left(\tilde{k}_f\frac{\partial\left\langle T_f\right\rangle^f}{\partial x_i}\right) + \phi\left\langle\tau_{ji}\frac{\partial u_i}{\partial x_j}\right\rangle^f + \alpha A_v\left(\left\langle T_s\right\rangle^s - \left\langle T_f\right\rangle^f\right), \tag{20}$$

$$\left\langle\rho_s\frac{dh_s}{dt}\right\rangle = \frac{\partial\left((1-\phi)\left\langle\rho_s\right\rangle^s\left\langle e_s\right\rangle^s\right)}{\partial t} = \frac{\partial}{\partial x_i}\left(\tilde{k}_s\frac{\partial\left\langle T_s\right\rangle^s}{\partial x_i}\right) + \alpha A_v\left(\left\langle T_f\right\rangle^f - \left\langle T_s\right\rangle^s\right). \tag{21}$$

Here, the operator $\langle\rangle$ denotes the volume averaging in an REV. $\langle\rangle^f$ and $\langle\rangle^s$ denote the volume averaging in the fluid or solid phase of an REV. The dispersion effect due to the coupling of two variables is neglected in these equations, e.g., it is assumed that $\phi\left\langle\rho_f u_i\right\rangle^f$ is identical to $\phi\left\langle\rho_f\right\rangle^f\left\langle u_i\right\rangle^f$. $\tilde{k}_f$ and $\tilde{k}_s$ in the energy Eqs. (20) and (21)are the effective thermal conductivities in the fluid and solid phases, respectively, which need to be modeled in a simulation. A_v is the volume averaged fluid-solid interface area. α is the heat transfer coefficient. F_i is the total drag by the porous matrix, which can be approximated using the Forchheimer extension of the Darcy law, expressed as,

$$F_i = \frac{\mu}{K}u_{Di} + \frac{c_F}{\sqrt{K}}\left|\mathbf{u}_D\right|u_{Di}, \tag{22}$$

where $u_{Di} = \phi\left\langle u_i\right\rangle^f$ is the superficial velocity. K is the permeability. c_F is the Forchheimer constant.

Multiplying Eq. (4) with u_i and performing the volume averaging, the transport equation for the macroscopic kinetic energy $\left\langle\rho_f k\right\rangle = \frac{1}{2}\left\langle\rho_f u_i u_i\right\rangle$ can be written as

$$\left\langle\rho_f\frac{dk}{dt}\right\rangle = \frac{\partial\left(\phi\left\langle\rho_f\right\rangle^f k_m\right)}{\partial t} + \frac{\partial\left(\phi\left\langle\rho_f\right\rangle^f\left\langle u_i\right\rangle^f k_m\right)}{\partial x_i} = -\phi\left\langle u_i\right\rangle^f\frac{\partial\langle p\rangle^f}{\partial x_i} + \phi\left\langle u_i\right\rangle^f\frac{\partial\left\langle\tau_{ji}\right\rangle^f}{\partial x_j} + \phi\left\langle\rho_f\right\rangle^f\left\langle u_i\right\rangle^f g_i + \phi\left\langle u_i\right\rangle^f F_i. \tag{23}$$

Here $\langle \rho_f k \rangle$ is approximated with $\phi \langle \rho_f \rangle k_m$, where $k_m = \frac{1}{2}\langle u_i \rangle^f \langle u_i \rangle^f$, as the dispersion part of $\rho_f \langle k \rangle^f$ is neglected. In addition, it is assumed that the loss of the kinetic energy is dominated by the drag force by the porous matrix F_i. Thus, the viscous heat $\phi \left\langle \tau_{ji} \frac{\partial u_i}{\partial x_j} \right\rangle^f$ in the macroscopic energy Eq. (20) is approximated with $\phi \langle u_i \rangle^f F_i$.

The macroscopic entropy generation intensities in the flow and temperature fields can be directly calculated by averaging s_{fD}^{gen} and $s_{fC}^{gen} + s_{sC}^{gen}$ in an REV. However, this requires the flow and temperature fields to be resolved in pores, which is extremely expensive. Here, we propose a macroscopic entropy transport equation, in which the macroscopic entropy generation intensity is modeled: Taking volume average of $\rho_f \frac{ds_f}{dt} + \rho_s \frac{ds_s}{dt}$ and considering Eqs. (10) and (11)

$$\left\langle \rho_f \frac{ds_f}{dt} + \rho_s \frac{ds_s}{dt} \right\rangle = \left\langle \frac{\rho_f}{T_f}\frac{dh_f}{dt} - \frac{1}{T_f}\frac{dp}{dt} + \frac{\rho_s}{T_s}\frac{dh_s}{dt} \right\rangle \tag{24}$$

is obtained. If the spatial variation of T_f and T_s in an REV is considered small, Eq. (24) can be further decoupled as

$$\left\langle \rho_f \frac{ds_f}{dt} + \rho_s \frac{ds_s}{dt} \right\rangle = \frac{1}{\langle T_f \rangle^f} \left\langle \rho_f \frac{dh_f}{dt} - \frac{dp}{dt} \right\rangle + \frac{1}{\langle T_s \rangle^s} \left\langle \rho_s \frac{dh_s}{dt} \right\rangle. \tag{25}$$

Substituting Eqs. (20) and (21) into Eq. (25), the macroscopic transport equation of entropy can be expressed as

$$\begin{aligned} \left\langle \rho_f \frac{ds_f}{dt} + \rho_s \frac{ds_s}{dt} \right\rangle &= \frac{\partial}{\partial x_i}\left(\frac{\tilde{k}_f}{\langle T_f \rangle^f} \frac{\partial \langle T_f \rangle^f}{\partial x_i} + \frac{\tilde{k}_s}{\langle T_s \rangle^s} \frac{\partial \langle T_s \rangle^s}{\partial x_i} \right) \\ &+ \alpha A_v \frac{\left(\langle T_s \rangle^s - \langle T_f \rangle^f \right)^2}{\langle T_s \rangle^s \langle T_f \rangle^f} \\ &+ \frac{\tilde{k}_f}{\langle T_f \rangle^{f2}} \frac{\partial \langle T_f \rangle^f}{\partial x_i} \frac{\partial \langle T_f \rangle^f}{\partial x_i} \\ &+ \frac{\tilde{k}_s}{\langle T_s \rangle^{s2}} \frac{\partial \langle T_s \rangle^s}{\partial x_i} \frac{\partial \langle T_s \rangle^s}{\partial x_i} + \frac{\phi \langle u_i \rangle^f F_i}{\langle T_f \rangle}. \end{aligned} \tag{26}$$

Eq. (26) indicates that entropy is generated in an isolated system due to heat transfer between the fluid and solid phases, heat transfer within the fluid and solid phases, and pressure drop (or dissipation) in the flow field. The corresponding entropy generation intensities $\dot{s}_{hsf}^{mac}$, $\dot{s}_{hts}^{mac}$, $\dot{s}_{htf}^{mac}$ and $\dot{s}_{pre}^{mac}$ are

$$\dot{s}_{hsf}^{mac} = \alpha A_v \frac{\left(\langle T_s \rangle^s - \langle T_f \rangle^f \right)^2}{\langle T_s \rangle^s \langle T_f \rangle^f}, \tag{27}$$

$$\dot{s}_{htf}^{mac} = \frac{\tilde{k}_f}{\langle T_f \rangle^{f2}} \frac{\partial \langle T_f \rangle^f}{\partial x_i} \frac{\partial \langle T_f \rangle^f}{\partial x_i}, \tag{28}$$

$$\dot{s}_{hts}^{mac} = \frac{\tilde{k}_s}{\langle T_s \rangle^{s2}} \frac{\partial \langle T_s \rangle^s}{\partial x_i} \frac{\partial \langle T_s \rangle^s}{\partial x_i}, \tag{29}$$

and

$$\dot{s}_{pre}^{mac} = \frac{\phi \langle u_i \rangle^f F_i}{\langle T_f \rangle}, \tag{30}$$

respectively. Eq. (30) assumes that the mechanical energy loss due to the Darcy–Forchheimer drag is dissipated as internal energy at the local fluid temperature T_f, analogous to the dissipation of kinetic energy.

Similarly, taking volume average of $\rho_f \frac{db_f}{dt} + \rho_s \frac{db_s}{dt}$ and considering Eqs. (14) and (15), there is

$$\left\langle \rho_f \frac{db_f}{dt} + \rho_s \frac{db_s}{dt} \right\rangle = \left\langle \rho_f \frac{dh_f}{dt} + \rho_s \frac{dh_s}{dt} - T_0 \left(\rho_f \frac{ds_f}{dt} + \rho_s \frac{ds_s}{dt} \right) + \rho_f \frac{dk}{dt} \right\rangle. \tag{31}$$

Substituting Eqs. (20), (21), (23) and (26) into Eq. (31), the following macroscopic transport equation of exergy can be obtained and expressed as,

$$\begin{aligned} \left\langle \rho_f \frac{db_f}{dt} + \rho_s \frac{db_s}{dt} \right\rangle &= \phi \frac{\partial \langle p \rangle^f}{\partial t} + \frac{\partial}{\partial x_i}\left(\tilde{k}_f \left(1 - \frac{T_0}{\langle T_f \rangle^f} \right) \frac{\partial \langle T_f \rangle^f}{\partial x_i} \right) \\ &+ \frac{\partial}{\partial x_i}\left(\tilde{k}_s \left(1 - \frac{T_0}{\langle T_s \rangle^s} \right) \frac{\partial \langle T_s \rangle^s}{\partial x_i} \right) - T_0 \left(\dot{s}_{hsf}^{mac} + \dot{s}_{htf}^{mac} + \dot{s}_{hts}^{mac} + \dot{s}_{pre}^{mac} \right). \end{aligned} \tag{32}$$

Eq. (32) shows that, the exergy is destructed due to the entropy generation. The corresponding exergy loss coefficients are termed as thermal loss coefficient

$$\zeta_{hsf}^b = \frac{1}{B_{chg}} \int_{cyc} \int_{vol} \dot{I}_{hsf} dV dt = \frac{1}{B_{chg}} \int_{cyc} \int_{vol} T_0 \dot{s}_{hsf}^{mac} dV dt, \tag{33}$$

fluid conduction loss coefficient

$$\zeta_{htf}^b = \frac{1}{B_{chg}} \int_{cyc} \int_{vol} \dot{I}_{htf} dV = \frac{1}{B_{chg}} \int_{cyc} \int_{vol} T_0 \dot{s}_{htf}^{mac} dV dt, \tag{34}$$

solid conduction loss coefficient

$$\zeta_{hts}^b = \frac{1}{B_{chg}} \int_{cyc} \int_{vol} \dot{I}_{hts} dV = \frac{1}{B_{chg}} \int_{cyc} \int_{vol} T_0 \dot{s}_{hts}^{mac} dV dt, \tag{35}$$

and pressure loss coefficient

$$\zeta_{pre}^b = \frac{1}{B_{chg}} \int_{cyc} \int_{vol} \dot{I}_{pre} dV = \frac{1}{B_{chg}} \int_{cyc} \int_{vol} T_0 \dot{s}_{pre}^{mac} dV dt. \tag{36}$$

where B_{chg} represents the difference between the total exergy entering the tank during the charging process and that entering the tank during the discharging process. $\dot{I}_{hsf}$, $\dot{I}_{htf}$, $\dot{I}_{hts}$ and $\dot{I}_{pre}$ are the (local) exergy loss intensities due to the heat transfer between solid and fluid, heat transfer in the fluid, heat transfer in the solid and pressure loss, respectively. Integrating them in the tank volume yields the exergy loss rates $\dot{L}_{hsf}$, $\dot{L}_{htf}$, $\dot{L}_{hts}$ and $\dot{L}_{pre}$. Besides these losses that occur inside the porous medium, the exergy is also lost at the boundary surfaces. The corresponding loss coefficients are the exit loss coefficient (due to the outflow of the HTF at the bottom tank)

$$\zeta_{bot}^b = \frac{1}{B_{chg}} \int_{cyc} \dot{L}_{bot}^b dt = \frac{1}{B_{chg}} \int_{cyc} \int_{bot} \phi \langle \rho_f \rangle^f \langle u_i \rangle^f \langle b_f \rangle^f n_i dA dt, \tag{37}$$

and the heat leakage loss coefficient (due to the heat release at the wall surfaces)

$$\zeta_{wal}^b = \frac{1}{B_{chg}} \int_{cyc} \dot{L}_{wal}^b dt = \frac{1}{B_{chg}} \int_{cyc} \int_{wal} \left(\tilde{k}_f \left(1 - \frac{T_0}{\langle T_s \rangle^f} \right) \frac{\partial \langle T_f \rangle^f}{\partial x_i} + \tilde{k}_s \left(1 - \frac{T_0}{\langle T_s \rangle^s} \right) \frac{\partial \langle T_s \rangle^s}{\partial x_i} \right) n_i dA dt. \tag{38}$$

The total exergy loss coefficient, denoted by

$$\zeta_{tot}^b = \zeta_{hsf}^b + \zeta_{htf}^b + \zeta_{hts}^b + \zeta_{pre}^b + \zeta_{bot}^b + \zeta_{wal}^b, \tag{39}$$

is the sum of the exergy loss coefficients due to the aforementioned mechanisms. These loss coefficients are termed to be consistent with the definitions by White, et al. (2016) [23], while they can be used to perform the SLA of multi-dimensional CFD results. The sources of modeling errors in the macroscopic equations arise from the assumptions made during the volume-averaging of the microscopic equations. These include the uncertainty of the REV size, modeling of the drag force F_i, the effective thermal conductivities $\tilde{k}_f$ and $\tilde{k}_s$, the interfacial heat transfer coefficient α, the neglection of the momentum and thermal dispersions, and the assumption that the pressure loss is entirely dissipated into internal energy.

2.3. Solver for macroscopic simulations and numerical methods

In this study the macroscopic Eqs. (18)–(21) are solved. The pore-scale geometry of the packed bed is modeled, rather than explicitly

Table 1
Main parameters used in the experiments by the PROMES-CNRS laboratory. The parameter with * is tentatively given in this study.

Energy	8.3 kWh$_T$
Discharge time t_{dis}	3 h
*Charge time t_{chg}	3 h
Tank height H	1.8 m
Tank diameter D	0.4 m
Tank volume V	0.23 m^3
Tank surface area A	2.26 m^2
Porosity ϕ	0.41
Particle diameter d_p	40 mm
Permeability K	1.76×10^{-6} m^2
HTF mass flow rate $\dot{m}$	0.019 kg m^{-1}
HTF high temperature T_H	483 K
HTF low temperature T_L	433 K

resolved, by employing a homogeneous porous medium assumption. Pore-scale geometry of the packed-bed is modeled, not directly resolved, with a homogenous porous-medium assumption. A finite volume method is used for the simulation. The solver is developed based on the conjugate heat transfer solver chtMultiRegionFoam from the open-source code package OpenFOAM 22.12. An Euler implicit scheme is used for the time discretization. A second-order central difference scheme is used for the convective terms in the momentum and energy equations of the fluid phase. A second order central difference scheme is used for the diffusion terms in both the fluid and solid phases. The solid and fluid regions completely overlap. The temperature of each phase is interpolated into the other phase to calculate the heat source term due to the heat transfer rate between the two phases. The same numerical schemes used for the fluid phase have also been applied in our previous studies on pore-scale resolved simulations of convection in porous media [29–32], as well as in macroscopic simulations [33,34]. In the present study, conjugate heat transfer between the fluid and solid phases is additionally considered. Therefore, further validation of the solver is performed.

3. Description of test cases and validation

To demonstrate the application of the SLA to system optimization, we have simulated the charge and discharge process of a laboratory-scale packed-bed SHS system. The experiment was performed in the PROMES-CNRS laboratory and reported in [6]. In the experiment, the storage tank, which is filled with quartzite rocks (TESM), is heated and cooled with rapeseed oil. The oil acts as the heat transfer fluid (HTF) and flows through the tank. A schematic illustration of the studied SHS system is shown in Fig. 1. The computational domain is assumed to be axi-symmetric to reduce the computational cost. The main parameters used in the experiments are shown in Table 1. The permeability K is calculated using the Carman–Konzeny equation [35], expressed as

$$K = \frac{d_p^2 \phi^3}{180\,(1-\phi)^2}. \tag{40}$$

The properties of the HTF and the TESM are shown in Table 2. The working fluid used in the experiments is liquid rapeseed oil, which is also adopted in the present simulations. Within the temperature range considered in this study (433–483 K), the density variation of the oil is approximately 4% relative to the reference value ($\rho_f = 804\,\mathrm{kg\,m^{-3}}$). Therefore, the fluid density is assumed to be constant in the present model, and buoyancy effects associated with temperature-dependent density variations are neglected.

The tank is insulated with $\delta_w = 20$ cm of rock wool covered with aluminum. The insulation effect is modeled at the wall surface. The corresponding boundary conditions for the fluid and solid phases are

$$\tilde{k}_f \mathbf{n}\cdot\boldsymbol{\nabla} T_f = \phi k_w \frac{T_o - T_{wf}}{\delta_w} = \phi\alpha_a \left(T_a - T_o\right), \tag{41}$$

Table 2
Thermal properties of the HTF and TESM.

HTF density ρ_f	804	kg m^{-3}
TESM density ρ_s	2500	kg m^{-3}
HTF heat capacity C_{pf}	$2086 - 0.84T_f$	J kg^{-1} K^{-1}
TESM heat capacity C_{ps}	830	J kg^{-1} K^{-1}
HTF heat conductivity k_f	$0.0981 - 2.4\times10^{-4}T_f$	W m^{-1} K^{-1}
TESM heat conductivity k_s	5.69	W m^{-1} K^{-1}
HTF dynamic viscosity μ_f	$0.02184 - 3.9\times0^{-5}T_f$	Pa s

Table 3
Boundary conditions used in the study.

	Velocity	Temperature (fluid)	Temperature (solid)	Pressure
Charge:				
Top	Zero-gradient	Constant T_H	Zero-gradient	Constant p_1
Bottom	Zero-gradient	Zero-gradient	Zero-gradient	Constant p_0
Wall	Slip	Eq. (41)	Eq. (42)	Zero-gradient
Discharge:				
Top	Zero-gradient	Zero-gradient	Zero-gradient	Constant p_0
Bottom	Zero-gradient	Constant T_C	Zero-gradient	Constant p_1
Wall	Slip	Eq. (41)	Eq. (42)	Zero-gradient

and

$$\tilde{k}_s \mathbf{n}\cdot\boldsymbol{\nabla} T_s = (1-\phi)\, k_w \frac{T_o - T_{ws}}{\delta_w} = (1-\phi)\,\alpha_a \left(T_a - T_o\right). \tag{42}$$

Here T_{wf} and T_{ws} are the inner wall surface temperatures of the fluid and solid phases, respectively. It is assumed that their difference is small. T_o is the external surface temperature of the insulation. T_a is the ambient temperature, which is assumed to be 300 K. According to the experimental study [6], the total thermal resistance between the storage tank and the ambient environment is reported to be in the range $R_{th} = 0.65 - 0.83\,\mathrm{KW^{-1}}$. In the present study, an intermediate value $R_{th} = 0.7\,\mathrm{KW^{-1}}$ is adopted. Using the tank surface area $A = 2.26$ m^2 (see Table 1), the corresponding heat transfer coefficient α_a can be calculated as $1/(A\,R_{th}) = 0.63$ Wm^{-2}K^{-1}.

A slip boundary condition is applied at the tank boundary walls. The viscous layer near the wall surfaces is neglected since its effect is limited to a very thin boundary layer close to the wall [35]. Table 3 summarizes the boundary conditions in the simulations. The ambient pressure p_0 is set to the atmospheric pressure ($p_0 = 101325$ Pa). The inlet pressure p_1 is adjusted during the simulation to ensure that the prescribed mass flow rate is achieved (0.19 kg m^{-2} s^{-1} for the experimental case). The gravitational force is not considered explicitly since it can be combined with the pressure gradient term and it does not cause losses in energy or exergy. Initially, the velocity, temperature, and pressure fields are set to zero velocity, T_C, and p_0, respectively. A steady-state solver is first employed to compute the velocity and pressure fields. It is assumed that the flow field remains unchanged during the charging and discharging processes. Subsequently, the transient temperature field is calculated using an unsteady solver while keeping the flow field fixed.

The pressure, velocity, and energy residual tolerances are set to 10^{-6}, 10^{-12}, and 10^{-12} respectively. Three mesh resolutions are used to examine their effect on the numerical simulations, corresponding to 100 (mesh A), 150 (mesh B), and 200 (mesh C) mesh cells per meter. Fig. 2a shows the time evolution of the HTF temperature at the tank centerline obtained using the three mesh resolutions. The numerical results change slightly when the mesh resolution is increased from mesh A to mesh B, while almost no difference is observed when the mesh resolution is further increased to mesh C. In addition, the numerical results obtained with time steps of $dt = 1$ s and 0.5 s are nearly identical. Based on the mesh resolution and time-step sensitivity study, mesh C and $dt = 1$ s are adopted in this study.

Each test case is computed using a single processor (Intel E5-2680v4 or AMD EPYC 9354) at the computing center of Hamburg University

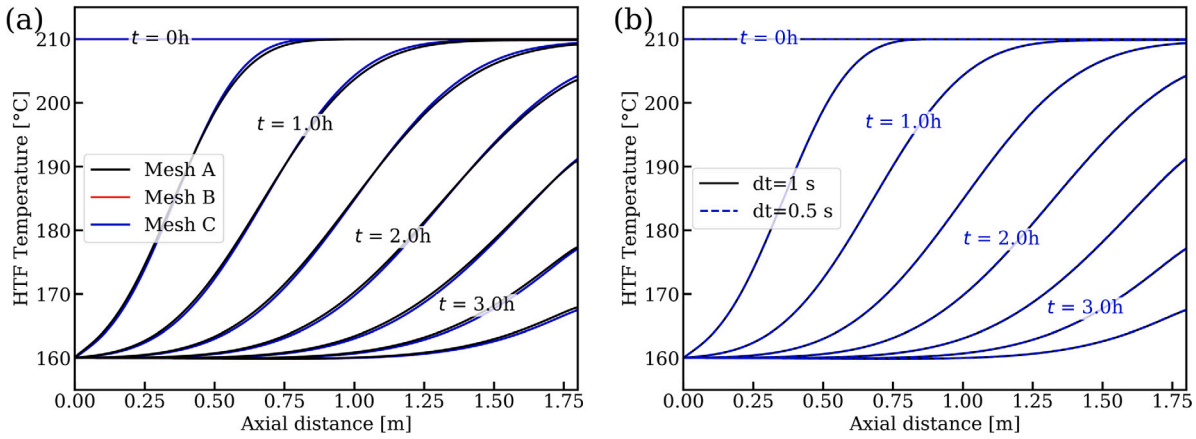

Fig. 2. Time evolution of the HTF temperature along the centerline. (a) Comparison of numerical results obtained with mesh A (20 × 180), mesh B (30 × 270), and mesh C (40 × 360). (b) Comparison of results obtained with time steps of dt = 1 s and 0.5 s.

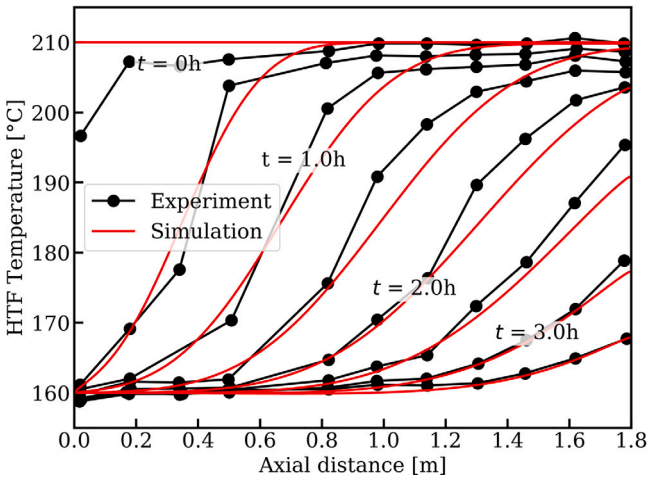

Fig. 3. Time evolution of the HTF temperature at the center line. The numerical results are compared with the experimental results in [6].

of Technology. The simulation of one complete cycle (charging and discharging) requires approximately 31 min of wall-clock time. Due to the relatively simple tank geometry and moderate grid size, the computational cost remains manageable even for transient multi-cycle simulations.

The numerical results are compared with the experimental data in [6], see Fig. 3. There is a slight discrepancy between the two results, as the experiment has not been fully represented in the simulation. For instance, the heat release at the wall is modeled using zero-dimensional Eqs. (41) and (42), while the heat conduction within the insulating walls is neglected. However, it is expected that this difference will not affect our analysis.

4. Results and discussion

The three-hour charging duration is adopted based on the experimental study of this test case [6], in which the storage tank is reported to be nearly fully charged after approximately three hours of operation. Therefore, the same charging duration is used in the present simulations to remain consistent with the experimental conditions. Since experimental data for the discharge process are not available, the discharge duration is also set to three hours for consistency. Additional numerical tests show that the storage tank is nearly fully discharged within this period. Similar to [27], we have neglected the heat released during the storing time between charge and discharge. Eleven charge–discharge cycles are calculated, see Fig. 4. A fully developed cycle, which is also called a steady-state cycle in [27], is obtained by the third cycle. The flow and temperature fields change periodically once the charge–discharge process is fully developed. We use the results of one fully developed cycle in our analysis. Fig. 5 shows the fluid temperature fields in a fully-developed charge–discharge cycle. For simplicity, the starting time of this cycle is set to t = 0 h, whose results are the same as those at the end of the cycle (t = 6 h). The thermocline indicated by the region between T_f = 455 K and T_f = 465 K can be clearly seen during the charge (t = 1 h and 2 h) and discharge (t = 4 h and 5 h). The thermocline in the solid phase is very similar to the thermocline in the fluid phase; therefore, they are assumed to be the same.

4.1. Energy and exergy loss coefficients

Fig. 6 shows the (thermal) energy and exergy loss rates during a fully developed cycle. The energy analysis shows that the primary energy losses occur at the system boundaries, due to heat release at the outlet during the charging process and heat leakage through the tank wall. The heat leakage loss ($\dot{L}^e_{wal}$) is considerably smaller than the exit loss ($\dot{L}^e_{bot}$) and remains relatively constant throughout the cycle. During the discharging process, the flow direction is reversed and the bottom boundary becomes the inlet, through which cold fluid enters the storage tank. Consequently, the heat loss associated with the outlet flow at the bottom no longer occurs. This change in the boundary condition leads to the sudden decrease in the energy and exergy loss rates observed after the charging stage in Fig. 6.

Losses in external system components (e.g., pipes, pumps, or heat exchangers outside the storage tank) are not included in the present analysis, since the focus of this study is the thermodynamic performance of the storage tank itself. In addition, as stated in [23], the exit loss cannot always be regarded as a real loss because the HTF leaving the tank may be utilized by other components in the cycle. This assumption is particularly relevant for integrated energy systems, such as concentrated solar power plants, where the outlet HTF from the storage tank can be directly supplied to downstream. In such cases, the exergy carried by the outlet flow can still be recovered and used within the overall system. By contrast, in standalone storage systems, where the outlet HTF is not directly utilized by other components, the exit exergy should be treated as a real thermodynamic loss. To account for this uncertainty, two limiting conditions are considered in the analysis. In the first case, the exit loss is treated as a pure loss from the storage system. In the second case, the exit exergy is assumed to be fully recoverable. These two assumptions provide upper and lower bounds for the thermodynamic losses associated with the outlet flow.

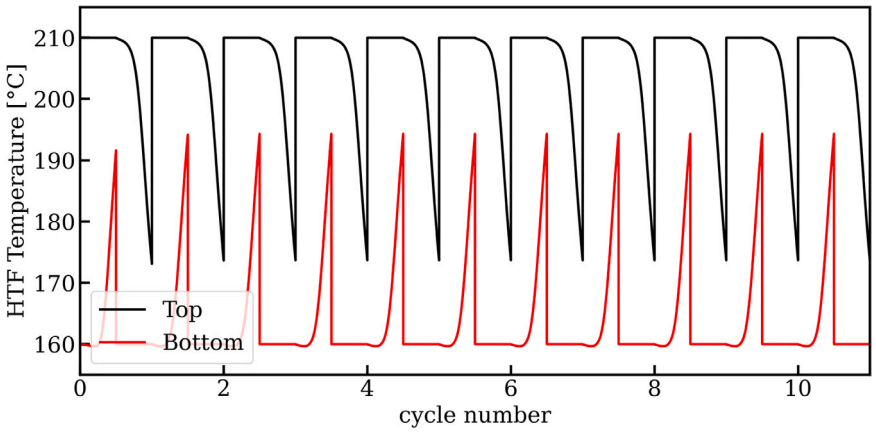

Fig. 4. Time evolution of the averaged HTF temperature at the top and bottom of the storage tank.

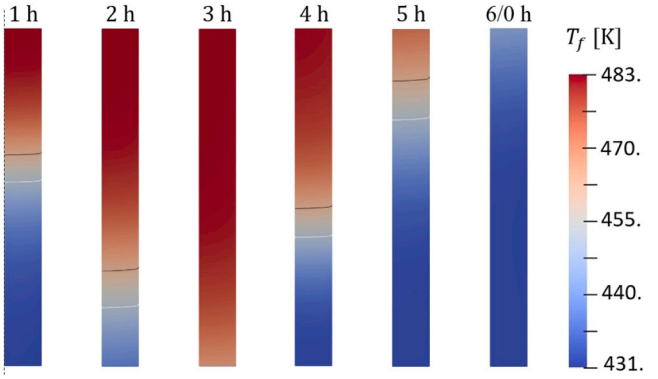

Fig. 5. Fluid temperature T_f fields during charge (0 h–3 h) and discharge (3 h–6 h). The iso-surfaces of $T = 463$ K (black lines) and $T = 453$ K (white lines) are shown to indicate the location of the thermocline. The axis of the tank is indicated at $T = 1$ h.

The internal flow and heat transfer processes do not lead to a net energy loss from the storage tank, but lead to internal irreversibilities, see Fig. 6b. These internal irreversibilities include thermal loss (due to heat transfer between the fluid and solid phases), fluid conduction loss (due to heat conduction in the fluid phase), solid conduction loss (due to heat conduction in the solid phase), and pressure loss associated with flow resistance. These loss mechanisms are quantified using Eqs. (33)–(36) based on the CFD results. The numerical results show that, besides the external losses, internal losses such as the thermal loss ($\dot{L}^b_{hsf}$) and the solid conduction loss $\dot{L}^b_{hts}$ are not negligible. Fig. 7 shows the internal losses in details. The thermal loss accounts for the largest share. This can be explained with the solid particles size used in the experiment. They are relatively large, which reduces the efficiency of heat transfer between the fluid and solid phases. In addition, the solid conduction loss ($\dot{L}^b_{hts}$) is more significant than the fluid conduction loss ($\dot{L}^b_{htf}$) because the thermal conductivity of the solid phase is higher than that of the fluid phase which leads to a higher entropy production (see (28), (29)) and hence a higher exergy loss. The pressure loss strongly depends on the mass flow rates considered, and thus on the corresponding velocities. In this particular case the pressure loss ($\dot{L}^b_{pre}$) is comparatively smalldue to the highly laminar flow and very low velocity. A comprehensive comparison of the energy and exergy loss coefficients is shown in Fig. 8, where the energy loss coefficients are calculated as $\zeta^e_{wal} = \frac{1}{Q_{chg}} \int_{cyc} \dot{L}^e_{wal} dt$ and $\zeta^e_{bot} = \frac{1}{Q_{chg}} \int_{cyc} \dot{L}^e_{bot} dt$.

Based on the numerical results, we can determine where the losses occur and how strong they are. It is already known that the exit loss occurs at the bottom of the tank and the heat leakage loss occurs at the wall surface. The other losses occur within the tank. Fig. 9 shows the instantaneous exergy loss intensities, $\dot{b}^b_{hsf}$ and $\dot{b}^b_{hts}$, at typical time instants during the charge ($t = 1, 2, 3$ h) and discharge ($t = 4, 5, 6$ h) processes. As can be seen in the figure, the thermal and the solid conduction losses occur very close to the thermocline indicated by the region between the iso-surfaces of $T = 455$ K and $T = 465$ K. Both $\dot{b}^b_{hsf}$ and $\dot{b}^b_{hts}$ are larger near the beginning of the charge or discharge processes, suggesting stronger heat transfer during these periods. The thermocline moves slightly faster than $\dot{b}^b_{hsf}$ and $\dot{b}^b_{hts}$. This occurs because the heat transfer between the fluid and solid, as well as the heat conduction within the solid, only happen once the surrounding fluid has reached a high temperature. Additionally, it can be also seen that the thermocline is slightly inclined to the wall surface, which is due to the heat release at the wall.

4.2. Effect of tank aspect ratio

To reduce the total (energy or exergy) loss, we have kept the tank volume at the original value $V = 0.23\,\mathrm{m}^3$, then studied the effect of the tank aspect ratio D/H on the loss coefficients. The studied tank diameter D ranges from 0.4 m to 1.2 m. The corresponding tank height ranges from 1.8 m to 0.2 m. Fig. 10 shows that, the energy exit loss coefficient ζ^e_{bot} increases as D increases. This is because that increasing the tank diameter reduces the fluid velocity, which weakens the heat transfer between the fluid and solid phases. Meanwhile, the heat leakage loss coefficient ζ^e_{wal} decreases as the wall surface area decreases. The energy analysis favors a low tank aspect ratio D/H for the parameters under consideration. It is expected that there is a minimum value of ζ^e_{tot} at a vary small tank diameter, which is not considered in this study. Note that this study does not consider the storage time between the end of charging and the start of discharging. If this is taken into account, the heat leakage loss could be more significant.

The trend of the exergy loss coefficient ζ^b_{tot} is similar to that of ζ^e_{tot} since the exit loss dominates the total loss, see Fig. 10b. However, if the exit loss is not considered a real loss, then the other losses become significant, see Fig. 11. Among the irreversible losses, the heat leakage loss coefficient ζ^b_{wal} decreases as D increases, while the conduction loss coefficients ζ^b_{hts} and ζ^b_{htf} increase due to the large cross-section of the thermocline. The exergy thermal loss is influenced by two competing effects: a reduced heat transfer coefficient between the solid and fluid phases tends to decrease entropy generation, while an increased temperature difference between the solid and fluid phases enhances irreversibility. As a result of these competing mechanisms, the thermal loss coefficient ζ^b_{hsf} exhibits a minimum value at $D = 0.8$ m and $H = 0.45$ m. These losses lead to an optimal tank diameter of $D_{opt} = 0.6$ m and an optimal tank height of $H_{opt} = 0.8$ m ($D_{opt}/H_{opt} =$

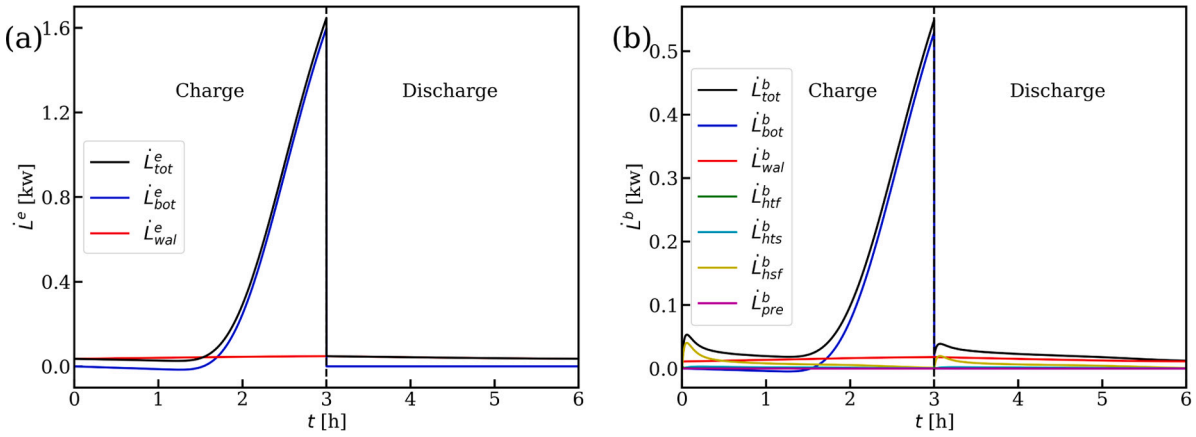

Fig. 6. Energy (a) and exergy (b) loss rates due to different mechanisms in a fully-developed charge–discharge cycle.

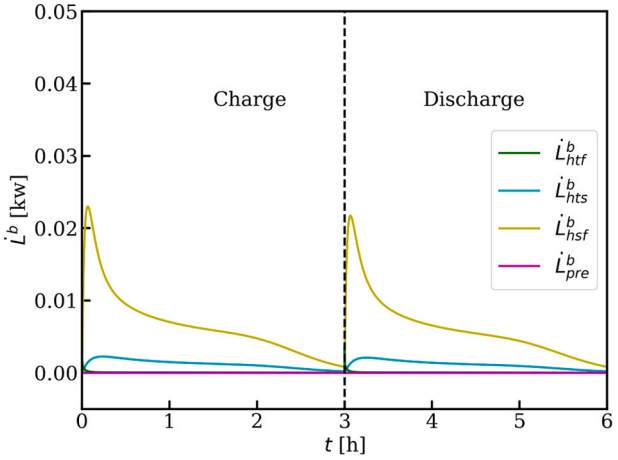

Fig. 7. Internal exergy loss rates due to different mechanisms in a fully-developed charge–discharge cycle.

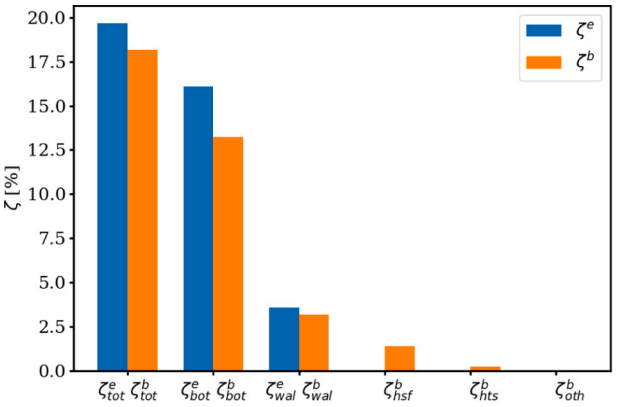

Fig. 8. Total energy and exergy loss coefficients and those due to different mechanisms.

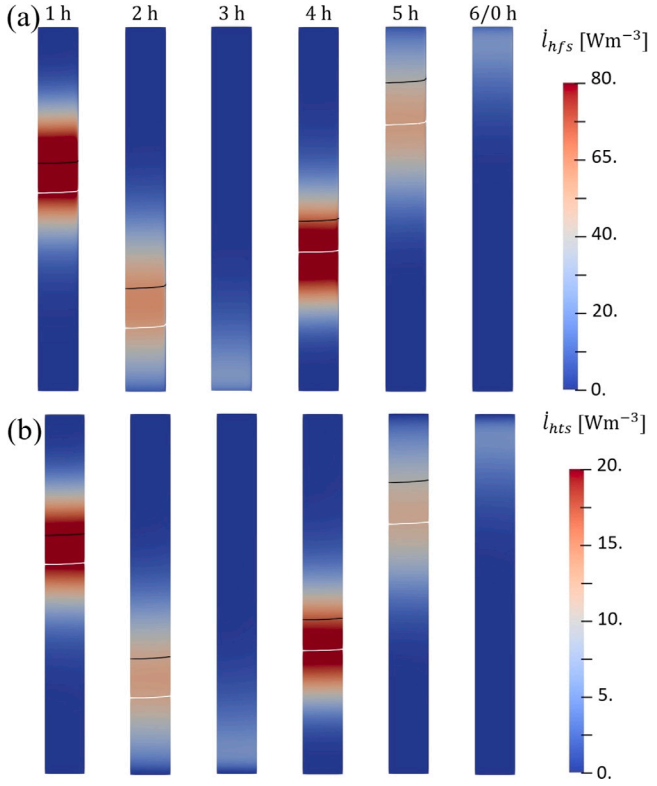

Fig. 9. Thermal loss intensity $\dot{i}_{hsf}$ (a) and solid conduction loss intensity $\dot{i}_{hts}$ for the original storage tank during the charge (0h–3h) and discharge (3h–6h). The iso-surfaces of T = 463K (black lines) and T = 453K (white lines) are shown to indicate the location of the thermocline.

0.75). Through optimization, the total loss coefficient ζ^b_{tot} is minimized to 4.5%, whereas ζ^b_{tot} for the original storage tank is 4.9%.

Fig. 12 shows the locations and strengths of the thermal and solid conduction losses in the optimized storage tank. Compared to the original storage tank, the thermal loss intensity is weaker in the optimized tank, while the solid conduction loss becomes stronger, see Figs. 9 and 12 for comparison. The thermocline still moves faster than the regions loss, however the lag is less evident.

4.3. Effect of particle size

The particle size d_p significantly affects energy or exergy losses. On the one hand, decreasing d_p enhances the heat transfer of the fluid and solid. This reduces the exit and thermal losses, thus improving the efficiency of a TES system. However, a decrease in d_p also causes a larger pressure loss, reducing the exergy storage efficiency η_{II}. Therefore, a SLA of the effect of d_p on a SHS system often yields an optimal d_p, which results in a minimum total loss coefficient ζ^b_{tot}.

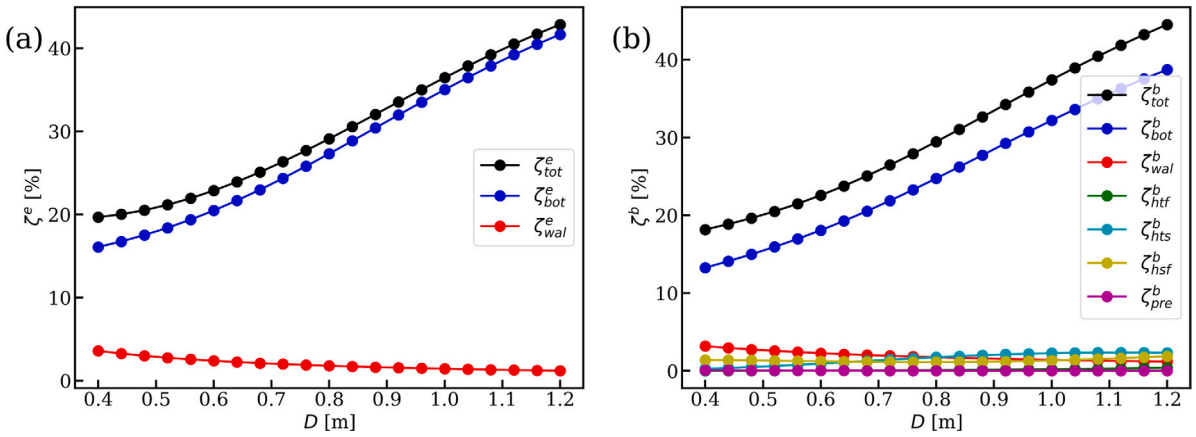

Fig. 10. Effect of the tank diameter D on the energy (a) and exergy (b) loss coefficients due to different mechanisms. The tank volume is kept as a constant (0.23 m^3). The exit loss is taken into account in the total loss.

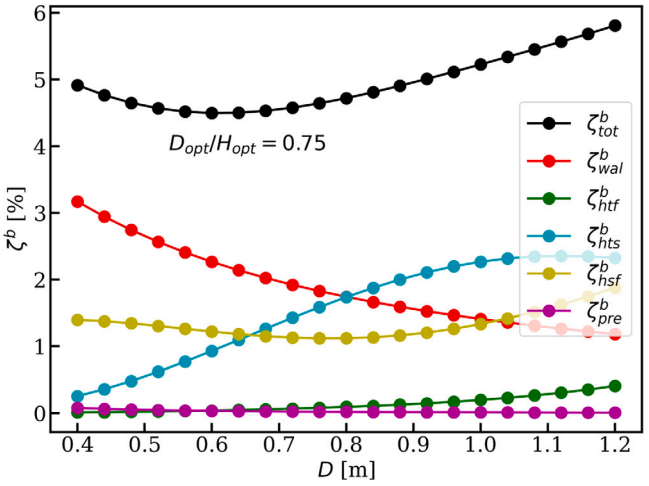

Fig. 11. Effect of the tank diameter D on the exergy loss coefficients due to different mechanisms. The tank volume is kept constant (0.23 m^3). The exit loss is not taken into account in the total loss.

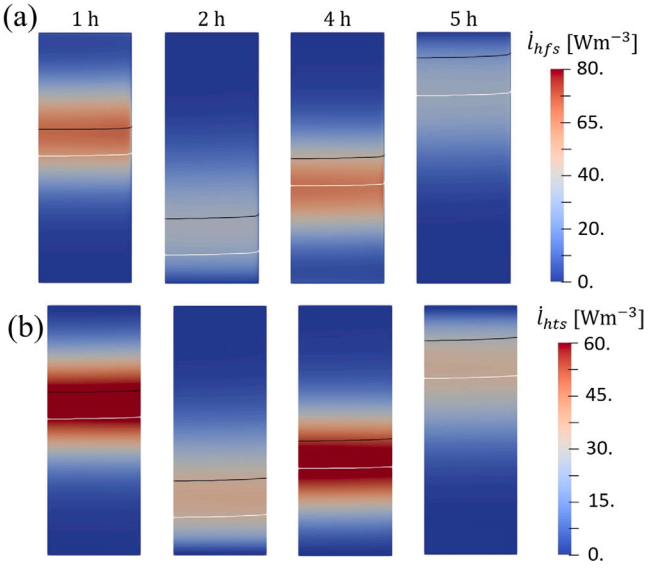

Fig. 12. Thermal loss intensity $\dot{i}_{hsf}$ (a) and solid conduction loss intensity $\dot{i}_{hts}$ for the storage tank with $D/H = 0.75$ during the charge (0 h–3 h) and discharge (3 h–6 h). The iso-surfaces of $T = 463$ K (black lines) and $T = 453$ K (white lines) are shown to indicate the location of the thermocline.

However, the SLA of the present TES system does not provide an optimized d_p value, see Fig. 13. The total energy loss coefficient ζ^e_{tot} and the exergy loss coefficient ζ^b_{tot} both decrease as d_p decreases. This is because the pressure loss in the current storage tank is very small due to the low flow velocity ($v = 8.4 \times 10^{-5}$ m/s for the optimized tank). Using the particles with their original size ($d_p = 40$ mm) results in a pressure drop of only 0.08 Pa, while reducing the particle size to 2 mm increases the pressure drop to 30.4 Pa, which remains relatively low. The pressure loss is significantly smaller than the other losses. Consequently, we have not identified an optimized d_p that minimizes the total exergy loss coefficient ζ^b_{tot}.

The total exergy loss coefficient ζ^b_{tot} does not provide an optimized particle size either when the exit loss is not considered, as shown in Fig. 14. As the tank's aspect ratio D/H decreases from 0.75 to 0.22 (the original value), the total exergy loss coefficient still decreases with a decrease in d_p, but more sharply (Fig. 15). However, since considering ζ^b_{tot} decreases very slowly with a decrease in d_p when $d_p \leq 8$ mm, we use the particles with $d_p = 8$ mm in our optimization. Fig. 16 shows that the thermal loss intensity weakens further as the particle size decreases, while the solid conduction loss intensity increases. Additionally, it can be seen that the thermocline becomes more parallel after the optimization, suggesting that the effect of the heat leakage at the wall becomes smaller.

4.4. Truncated-cone-shaped storage tanks

Based on the multi-dimensional CFD results, we can optimize the tank geometry to further improve the storage efficiency. One option for the shape optimization is replacing the current cylindrical tank with a truncated cone-shaped tank. The tank volume and height are kept constant at $V = 0.23\,m^3$ and $H = 0.8$ m. The truncated cone has an upper surface diameter D_1 and a lower surface diameter D_2. We define an equivalent diameter D_0 as the diameter of a cylinder with the same volume and height as the truncated cone. For the cylinder optimized in Section 4.2, the equivalent diameter is $D_0 = 0.8$ m. In this study, we have investigated D_1 in the range of 0.4 m to 1.0 m ($0.33 \leq D_1/D_0 \leq 1.67$).

The effect of the diameter ratio D_1/D_0 on the energy and exergy loss coefficients is shown in Fig. 17. The exit loss is taken into account in the total loss in these figures. D_1/D_0 affects the spatial distribution of the heat transfer coefficient and thus the entropy generation inside the tank. The CFD results show that a slightly larger top diameter improves the heat transfer in the colder region of the tank and reduces the total energy or exergy loss coefficients. The minimum energy loss coefficient, $\zeta^e_{tot} = 18.8\%$, is obtained as D_1 is set to the optimal value $D_{1,opt} = 0.64\,m$ ($D_{1,opt}/D_0 = 1.07$). However, the SLA suggests a slightly higher optimal

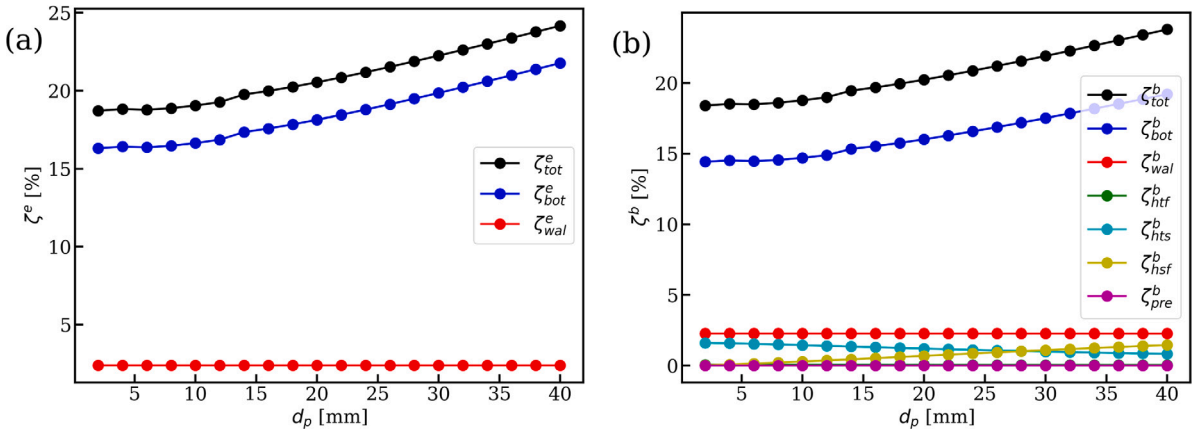

Fig. 13. Effect of the particle size d_p on the energy (a) and exergy (b) loss coefficients due to different mechanisms. The tank height and diameter are $H = 0.8\,\text{m}$ and $D = 0.6\,\text{m}$ ($D/H = 0.75$). The exit loss is taken into account in the total loss.

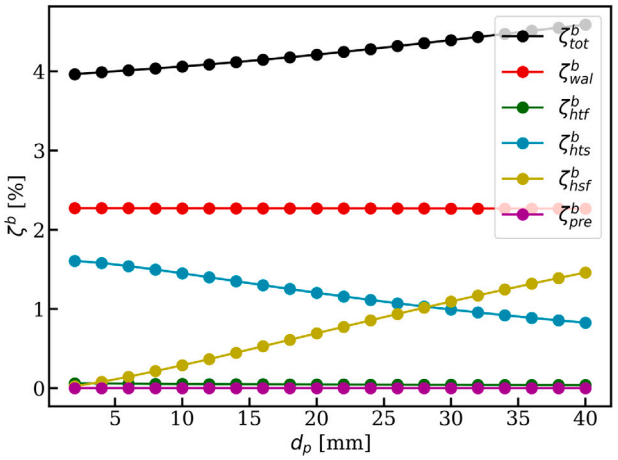

Fig. 14. Effect of the particle size d_p on the exergy loss coefficients due to different mechanisms. The tank height and diameter are $H = 0.8\,\text{m}$ and $D = 0.6\,\text{m}$ ($D/H = 0.75$). The exit loss is not taken into account in the total loss.

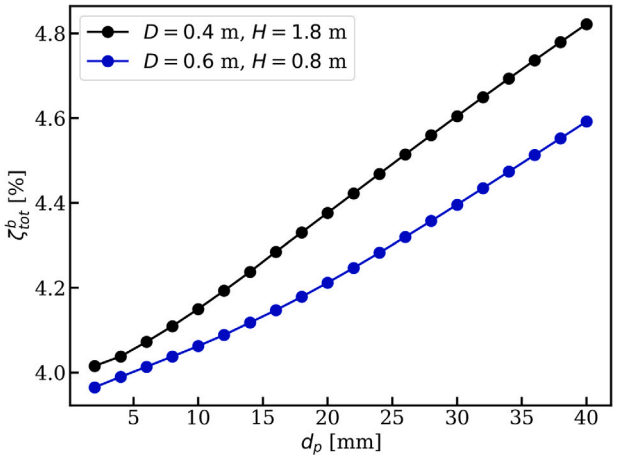

Fig. 15. Particle size d_p versus total exergy loss coefficients for different tank height-diameter ratios. The exit loss is not taken into account in the total loss.

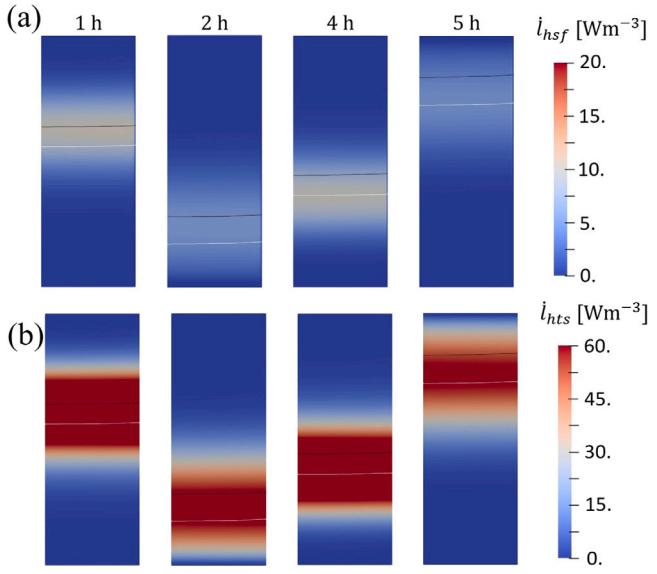

Fig. 16. Thermal loss intensity $\dot{i}_{hsf}$ (a) and solid conduction loss intensity $\dot{i}_{hts}$ for the storage tank with $D/H = 0.75$ and $d_p = 8\,\text{mm}$ during charge (0 h–3 h) and discharge (3 h–6 h). The iso-surfaces of $T = 463$ K (black lines) and $T = 453$ K (white lines) are shown to indicate the location of the thermocline.

value of $D_{1,opt} = 0.68\,m$ ($D_{1,opt}/D_0 = 1.13$). Additionally, ζ^b_{tot} increases very slowly as D_1 increases beyond its optimal value. The total energy and exergy exit loss coefficients at their optimal D_1 values are only slightly smaller than that of an equivalent cylindrical tank.

If the exit loss is not considered a real loss, then the optimal value of D_1 is $D_{1,opt} = 0.6\,m$ ($D_{1,opt}/D_0 = 1$), meaning the optimal geometry is a cylinder, see Fig. 18. This differs from the study of Li, et al. (2018) [14], who suggest that the truncated cone-shaped tank has better temperature stratification and thermal charging efficiency than cylindrical and spherical tanks. One possible reason of this discrepancy is that different HTF and THSM are used in this study, which may significantly affect on the optimal tank geometry. Additionally, a much more complicated heating system is studied in [14], which has a significant effect on the losses.

Fig. 19 shows the solid conduction loss intensity $\dot{i}_{hts}$ at typical times during a charge–discharge cycle. The change in $\dot{i}_{hts}$ is the most significant among internal losses when the exit loss is not considered, see Fig. 18. As can be seen, the solid conduction loss during discharge is much stronger than during charge. This is due to the strong thermal

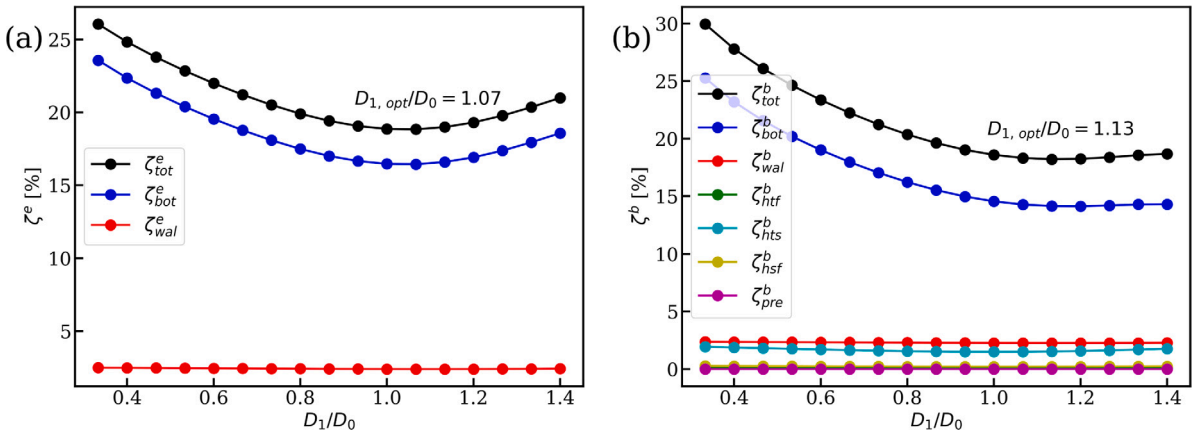

Fig. 17. Effect of the diameter ratio D_1/D_0 on the energy (a) and exergy (b) loss coefficients due to different mechanisms. The tank volume is kept as ($V = 0.23$ m). The exit loss is taken into account in the total loss.

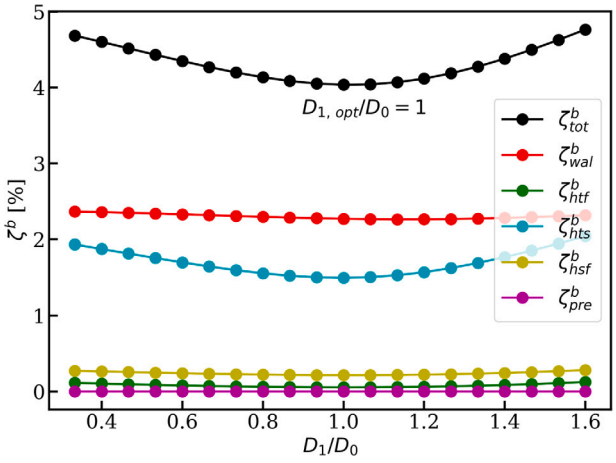

Fig. 18. Effect of the diameter ratio D_1/D_0 on the energy (a) and exergy (b) loss coefficients due to different mechanisms. The tank volume is kept as ($V = 0.23$ m). The exit loss is not taken into account in the total loss.

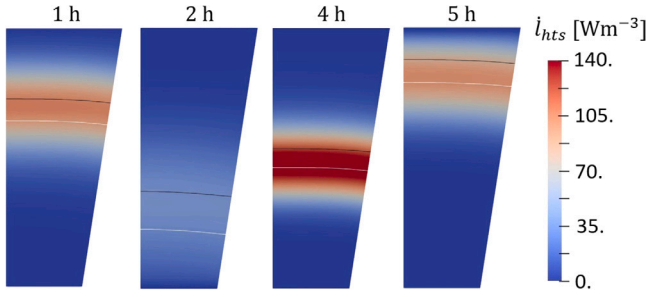

Fig. 19. Volume averaged exergy loss rates due to the heat transfer in the solid phase $\dot{i}_{hts}$ during charge (0 h–3 h) and discharge (3 h–6 h). The iso-surfaces of $T = 463$ K (black lines) and $T = 453$ K (white lines) are shown to indicate the location of the thermocline. The results for $D_1 = 0.68$ m, $D_2 = 0.48$ m, $H_{opt} = 0.8$ m and particle size ($d_{p,opt} = 8$ mm) are shown.

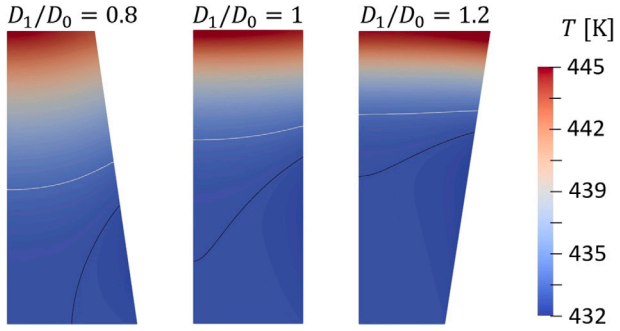

Fig. 20. Temperature fields for $D_1/D_0 = 0.8$, 1 and 1.2 at the end of discharge ($t = 6$ h). The white and black lines indicate the iso-surfaces of $T = 434$ K and 433 K, respectively.

conduction in the solid phase at the start of the discharge process. Another interesting phenomenon is that, as D_1/D_0 increases, the total energy loss coefficient ζ^e_{tot} increases beyond the optimal value, however, ζ^b_{tot} almost does not change. Fig. 20 shows the temperature fields at the end of the discharge process (or the start of the charge process) for three D_1/D_0 values (0.8, 1.0 and 1.2) and explains this phenomenon. On the one hand, the remaining energy in the tank after the discharge increases as D_1/D_0 increases. This results in a higher energy loss coefficient ζ^e during charging. However, the iso-surfaces of $T = 433$ K and 434 K shown in the figure suggest that, as D_1/D_0 increases, the temperature becomes more uniformly distributed near the tank bottom. This leads to higher entropy near the tank bottom, which reduces the exergy leaving the tank during charging. Fig. 21 shows the time evolution of the exit loss rate $\dot{L}^b_{bot}$ during the charge. It confirms that, as D_1/D_0 increases, $\dot{L}^b_{bot}$ is lower during the earlier discharge period and higher during the later period. This explains why ζ^b_{tot} changes very slightly as D_1/D_0 increases beyond its optimal value.

4.5. Final results of optimization

Summarizing the results above, we are able to optimize the packed-bed SHS system. If only an energy analysis is considered and the exit loss is excluded, the results suggest that reducing the tank height and the particle size would continuously improve the storage performance. In this case, no optimal design can be identified. In contrast, the second-law analysis (SLA) evaluates the destruction of available work and reveals the trade-offs between different loss mechanisms. Based on the main parameters shown in Table 1, we recommend using a truncated cone-shaped tank with height of $H_{opt} = 0.8$ m, an upper surface diameter of $D_{1,\,opt} = 0.68$ m and a lower surface diameter of $D_{2,\,opt} = 0.52$ m ($D_{1,\,opt}/D_0 = 1.13$). The tank is filled with the particles of $d_{p,\,opt} = 8$ mm, while the other parameters remain unchanged. Through optimization, the total exergy loss coefficient ζ^b_{tot} is reduced by approximately 16.3% from 4.9% to 4.1% when the exit loss is not considered a real loss. The

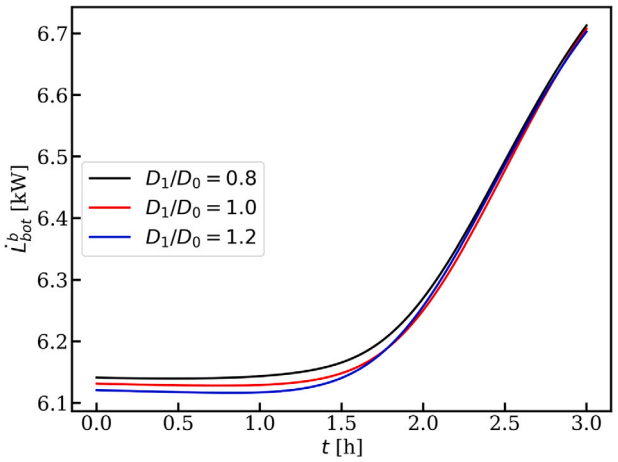

Fig. 21. Time evolution of the exit exergy loss rate $\dot{L}^b_{bot}$ for $D_1/D_0 = 0.8$, 1 and 1.2 during the charge.

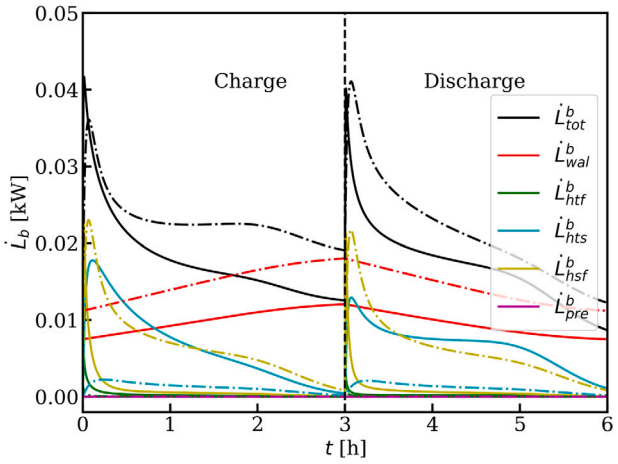

Fig. 22. Comparison of the exergy loss rate and its components for the original (dash-dotted lines) and optimized (solid lines) designs. The exit loss is not taken into account in the total loss.

comparison of the total exergy loss rate and its components for the original and optimized designs is shown in Fig. 22. As can be seen, the heat leakage loss ($\dot{L}^b_{wal}$) and the thermal loss ($\dot{L}^b_{hsf}$) are reduced through the optimization, while the solid conduction loss ($\dot{L}^b_{hts}$) increases.

When the exit loss is treated as a pure loss, the energy loss coefficient ζ^e_{tot} is slightly reduced from 19.7% to 19.0% in the optimized design, while ζ^b_{tot} is almost unchanged (18.6%). However, the exit exergy may be recoverable by downstream components and therefore does not necessarily represent a true thermodynamic loss. Under this assumption, the improvement achieved through the SLA-based optimization becomes is apparent. It is necessary to note that, the optimal design parameters obtained in this study are specific to the selected operating conditions, material properties, and boundary conditions. Variations in these parameters may lead to different optimal configurations. Additionally, the optimized tank geometry does not significantly increase manufacturing difficulty or introduce additional structural constraints compared with the original cylindrical design. The reduction of particle size does not lead to a significant increase in pressure drop. Replacing the cylindrical tank with a truncated-cone-shaped geometry may slightly increase manufacturing cost, which should be considered in practical design and fabrication.

5. Conclusions

In this study, we derived multi-dimensional macroscopic entropy and exergy transport equations for fluid flow and heat transfer in porous media from the microscopic transport equations. This derivation establishes a connection between pore-scale transport processes and the macroscopic fields used in continuum modeling. In contrast to previous second-law analyses of thermal energy storage systems, which are typically based on one-dimensional system simulations, the present formulation enables second-law analysis (SLA) using multi-dimensional CFD results and supports geometry optimization. It indicates where the irreversibility occurs and its strength. To our best knowledge, this derivation has not appeared in previous articles.

Using the laboratory scale packed-bed SHS system developed in the PROMES-CNRS laboratory as a test case, we have demonstrated how to perform a SLA with CFD results and optimize the design. The CFD results for this system show that energy loss primarily occurs at the tank bottom (exit loss) during charge and on the wall surface (heat leakage loss). In addition to the exit loss and the heat leakage loss, the SLA shows that thermal loss (due to heat transfer between the fluid and solid) and solid conduction loss (due to thermal conduction in the solid) are also significant contributors to the total exergy loss, while the other losses are negligible for the studied SHS system. Unlike the exit and heat leakage losses, which occur at the boundary surfaces, the thermal and solid conduction losses occur inside the tank, close to the thermocline. The thermocline moves faster than the regions where these losses occur. This results in a delay in the emergence of the losses.

The SLA framework developed in this study enables optimization of the storage tank geometry based on the global irreversible losses and their distribution, which has not been reported in previous studies either. The SLA of the present case suggests an optimized tank aspect ratio of $D_{opt}/H_{opt} = 0.75$, which yields a minimum total exergy loss coefficient ζ^b_{tot} as the exit loss is not considered as a real loss. As the exit loss is considered, both energy and exergy loss coefficients ζ^e_{tot} and ζ^b_{tot} decrease as D/H decreases, since this reduces the exit loss, which dominates the total loss. Additionally, both ζ^e_{tot} and ζ^b_{tot} decrease with d_p, regardless of whether the exit loss is considered. The pressure loss is negligible for the SHS system studied. The SLA recommends a tank with a truncated cone shape, with a slightly larger the upper surface ($D_{1,opt}/D_0 = 1.13$). This tank geometry yields the lowest value of ζ^b_{tot} as the exit loss is considered. Through the SLA, we have proposed a SHS system with a tank aspect ratio of $D_{opt}/H_{opt} = 0.75$, a diameter ratio of $D_{1,opt}/D_0 = 1.13$ and a particle size $d_{p,opt} = 8$ mm. Without considering the exit loss, the total exergy loss coefficient ζ^b_{tot} is reduced from 4.9% for the original design to 4.1% for the optimized design. It represents a relative reduction of about 16% in the total exergy destruction. In addition, the present test case represents a system with relatively small internal losses. In systems where irreversibilities are stronger, for example when compressed air is used as the HTF and the pressure loss becomes significant, the potential improvement achievable through second-law-based optimization is expected to be larger.

The study shows that the SLA is an effective tool for optimizing energy storage systems. Based on the SLA of multi-dimensional CFD results, we are able to identify where exergy is destroyed and how strong it is. This information provides useful guidance for improving system design. The proposed approach could be extended to other porous-medium-based storage configurations, such as radial-flow thermal energy storage systems. One limitation of the present model is that, applying the method to systems using phase change materials (PCM) may be more challenging, since such systems often involve moving phase boundaries and may not always be well represented by a homogeneous porous-medium model. Additionally, the computational cost may become significant for storage systems with complex geometries or strongly unsteady flow behavior. This is mainly because a wider range of geometric length scales may require finer mesh resolution and smaller time steps. These will be the focus of our future work.

Declaration of competing interest

The authors declare the following financial interests/personal relationships which may be considered as potential competing interests: Yan Jin reports financial support was provided by German Research Foundation. Yan Jin reports equipment, drugs, or supplies was provided by Hamburg University of Technology. If there are other authors, they declare that they have no known competing financial interests or personal relationships that could have appeared to influence the work reported in this paper.

Acknowledgments

The authors gratefully acknowledge the support of this study by the DFG, Germany (Deutsche Forschungsgemeinschaft, 552151258) and the computing center of Hamburg University of Technology (RZ-TUHH).

Data availability

Data will be made available on request.

References

[1] M. Medrano, A. Gil, I. Martorell, X. Potau, L.F. Cabeza, State of the art on high temperature thermal energy storage for power generation. Part 2 — case studies, Renew. Sustain. Energy Rev. 14 (1) (2010) 56–72.
[2] C. Zhang, J. Li, Y. Chen, Improving the energy discharging performance of a latent heat storage (LHS) unit using fractal-tree-shaped fins, Appl. Energy 259 (2020) 114102.
[3] A. Gil, et al., State of the art on high temperature thermal energy storage for power generation. Part 1 — concepts, materials and modelization, Renew. Sustain. Energy Rev. 14 (1) (2010) 31–55.
[4] U. Herrmann, B. Kelly, H. Price, Two-tank molten salt storage for parabolic trough solar power plants, Energy 29 (5–6) (2004) 883–893.
[5] F.G.F. Qin, et al., Thermocline stability criterions in single-tanks of molten salt thermal energy storage, Appl. Energy 97 (2012) 816–821.
[6] J.-F. Hoffmann, T. Fasquelle, V. Goetz, X. Py, A thermocline thermal energy storage system with filler materials for concentrated solar power plants: Experimental data and numerical model sensitivity to different experimental tank scales, Appl. Therm. Eng. 100 (2016) 753–761.
[7] C. Xu, Z. Wang, Y. He, X. Li, F. Bai, Parametric study and standby behavior of a packed-bed molten salt thermocline thermal storage system, Renew. Energy 48 (2012) 1–9.
[8] Y.F. Baba, A.A. Mers, H. Ajdad, Dimensionless model based on dual phase approach for predicting thermal performance of thermocline energy storage system: Towards a new approach for thermocline thermal optimization, Renew. Energy 153 (2020) 440–455.
[9] A.J. White, Loss analysis of thermal reservoirs for electrical energy storage schemes, Appl. Energy 88 (2011) 4150–4159.
[10] J.D. McTigue, A.J. White, Segmented packed beds for improved thermal energy storage performance, IET Renew. Power Gener. 10 (2016) 1498–1505.
[11] A. Zachar, I. Farkas, F. Szlivka, Numerical analyses of the impact of plates for thermal stratification inside a storage tank with upper and lower inlet flows, Sol. Energy 74 (4) (2003) 287–302.
[12] S. Göppert, R. Lohse, T. Urbaneck, U. Schirmer, B. Platzer, P. Steinert, New computation method for stratification pipes of solar storage tanks, Sol. Energy 83 (9) (2009) 1578–1587.
[13] B. Kurşun, Thermal stratification enhancement in cylindrical and rectangular hot water tanks with truncated cone and pyramid shaped insulation geometry, Sol. Energy 169 (2018) 512–525.
[14] A. Li, F. Cao, W. Zhang, B. Shi, H. Li, Effects of different thermal storage tank structures on temperature stratification and thermal efficiency during charging, Sol. Energy 173 (2018) 882–892.
[15] L. Gao, H. Lu, B. Sun, D. Che, L. Dong, Numerical and experimental investigation on thermal stratification characteristics affected by the baffle plate in thermal storage tank, J. Energy Storage 34 (2021) 102117.
[16] S.M. Hosseinnia, H. Akbari, M. Sorin, Numerical analysis of thermocline evolution during charging phase in a stratified thermal energy storage tank, J. Energy Storage 40 (2021) 102682.
[17] M. Cascetta, G. Cau, P. Puddu, F. Serra, A comparison between CFD simulation and experimental investigation of a packed-bed thermal energy storage system, Appl. Therm. Eng. 98 (2016) 1263–1272.
[18] M. Khan, N. Hassan, A. Azad, Investigation of thermal energy storage systems in concentrated solar power, Energy Procedia 160 (2019) 738–745.
[19] A. Andreozzi, B. Buonomo, O. Manca, S. Tamburrino, Thermal energy storages analysis for high temperature in air solar systems, Appl. Therm. Eng. 71 (1) (2014) 130–141.
[20] K.E. Elfeky, A.G. Mohammed, Q. Wang, Performance analysis of an air rock thermocline TES tank for concentrated solar power plants using the coupled DEM–cfd approach, Clean Technol. Env. Policy (2021) 1–17.
[21] T. Chekifi, M. Boukraa, CFD applications for sensible heat storage: A comprehensive review of numerical studies, J. Energy Storage 68 (2023) 107893.
[22] A. White, J. McTigue, C. Markides, Wave propagation and thermodynamic losses in packed-bed thermal reservoirs for energy storage, Appl. Energy 130 (2014) 648–657.
[23] A.J. White, J.D. McTigue, C.N. Markides, Analysis and optimisation of packed-bed thermal reservoirs for electricity storage applications, Proc. Inst. Mech. Eng. Part A: J. Power Energy 230 (7) (2016) 739–754.
[24] J.D. McTigue, A.J. White, C.N. Markides, Parametric studies and optimisation of pumped thermal electricity storage, Appl. Energy 137 (2015) 800–811.
[25] A. Abdulla, K.S. Reddy, Effect of operating parameters on thermal performance of molten salt packed-bed thermocline thermal energy storage system for concentrating solar power plants, Int. J. Therm. Sci. 121 (2017) 30–44.
[26] J. McTigue, A. White, A comparison of radial-flow and axial-flow packed beds for thermal energy storage, Appl. Energy 227 (2018) 533–541.
[27] J.D. McTigue, C.N. Markides, A.J. White, Performance response of packed-bed thermal storage to cycle duration perturbations, J. Energy Storage 19 (2018) 379–392.
[28] H. Herwig, The role of entropy generation in momentum and heat transfer, J. Heat Transf. 134 (3) (2012) 031003.
[29] S. Gasow, Z. Lin, H. Zhang, A. Kuznetsov, M. Avila, Y. Jin, Effects of pore scale on the macroscopic properties of natural convection in porous media, J. Fluid Mech. 891 (2020) A25.
[30] S. Gasow, A. Kuznetsov, M. Avila, Y. Jin, A macroscopic two-length-scale model for natural convection in porous media driven by a species-concentration gradient, J. Fluid Mech. 926 (2021) A8.
[31] S. Gasow, A. Kuznetsov, Y. Jin, Prediction of pore-scale-property dependent natural convection in porous media at high Rayleigh numbers, Int. J. Therm. Sci. 179 (2022) 107635.
[32] Y. Jin, A pore-scale resolved direct numerical simulation study for scaling analysis of the solutal convection in porous, J. Fluid Mech. 1000 (2024) A21.
[33] F. Rao, A. Kuznetsov, Y. Jin, Numerical modeling of momentum dispersion in porous media based on the pore scale prevalence hypothesis, Transp. Porous Media 133 (2020) 271–292.
[34] F. Rao, Y. Jin, Possibility for survival of macroscopic turbulence in porous media with high porosity, J. Fluid Mech. 937 (2022) A17.
[35] D.A. Nield, A. Bejan, Convection in Porous Media, fifth ed., Springer, Switzerland, 2017.